Texture-based ferroelectric hardening in $Na_{1/2}Bi_{1/2}TiO_3$-based piezoceramics

Daniel Bremecker [1,*] Andreas Wohninsland [1] Siegfried Teuber,[1] K. V. Lalitha, Manuel Hinterstein,[2] and Jürgen Rödel [1,†]

[1]*Division of Nonmetallic-Inorganic Materials, Department of Materials and Earth Sciences, Technical University of Darmstadt, 64287 Darmstadt, Germany*

[2]*Fraunhofer IWM, Freiburg, Germany and Institute for Applied Materials, Karlsruhe Institute of Technology, Karlsruhe, Germany*

(Received 2 March 2023; accepted 27 April 2023; published 16 June 2023)

$Na_{1/2}Bi_{1/2}TiO_3$-based (NBT-based) ceramics offer a viable option to replace lead-based materials for high-power applications as they are characterized by a stable mechanical quality factor with increasing vibration velocity in comparison to lead-based piezoceramics. Recently, the minor and stable extrinsic contributions were revealed as the origin for the stability of the mechanical quality factor with increasing vibration velocity. This work identifies the very unusual high poling degree as cause for the small extrinsic contributions. To this end, complete pole figure densities have been quantified and correlated to the piezoelectric coefficient and electromechanical quality factor. This hypothesis is further strengthened by correlating the piezoelectric constant (sum of intrinsic and extrinsic contributions) with the remanent polarization (correlates to remanent texturing degree). In order to assess a full picture of NBT-based piezoceramics, $0.94Na_{1/2}Bi_{1/2}TiO_3$-$0.06BaTiO_3$ has been considered with and without Zn doping and with quenching. It is compared to $0.79Na_{1/2}Bi_{1/2}TiO_3$-$0.21\ K_{1/2}Bi_{1/2}TiO_3$ with and without Mg doping. Finally, a contrast to soft $Pb(Zr_{1/2}Ti_{1/2})O_3$ (PZT) flushes out the impact of domain wall motion on the piezoelectric coefficient and the electromechanical quality factor. Whereas a PZT-based reference material exhibits a linear increase in the piezoelectric constant with increasing remanent polarization, the NBT-based materials deviate from the linear trend, indicating a decrease in extrinsic contributions.

DOI: 10.1103/PhysRevMaterials.7.064407

I. INTRODUCTION

The search for replacement of $Pb(Zr_xTi_{1-x})O_3$ (PZT) has been a long ongoing process [1–3]. An excellent opportunity to replace and even surpass PZT lies in the field of high-power applications. This field has received both enhanced scientific attention and increasing demand from application [4,5]. In this regard, $Na_{1/2}Bi_{1/2}TiO_3$-based (NBT) materials are considered as the best alternative for PZT [6–8]. They exhibit a stable mechanical quality factor Q_m with increasing vibration velocity v [9]. Two promising candidates are the lead-free solid solutions 1–$x(Na_{1/2}Bi_{1/2}TiO_3)$-$x(BaTiO_3)$ and 1–$x(Na_{1/2}Bi_{1/2}TiO_3)$-$x(K_{1/2}Bi_{1/2}TiO_3)$ (NBT-x100BT, NBT-x100KBT). Both form a morphotropic phase boundary (MPB), separating tetragonal and rhombohedral regions [10,11]. The highest piezoelectric activity is found around the MPB, where the tetragonal and rhombohedral phases coexist, both in the unpoled and poled states. NBT-xBT exhibits a piezoelectric coefficient, d_{33}, of 125–167 pC/N at 6–7 mol % BT [10,12] and NBT-xKBT features a d_{33} of 134–190 pC/N around 19–22 mol % KBT [13–15]. At the MPB, both materials are nonergodic relaxors, meaning a nonreversible ferroelectric state can be induced by application of an electric field or mechanical stress [16,17]. Above the respective ferroelectric to relaxor transition temperature, T_{F-R}, the field-induced ferroelectric state transitions into an ergodic relaxor state. In the literature, T_{F-R} at the MPB varies from 102 °C to 120 °C in NBT-6BT-NBT-7BT and from 120 °C to 135 °C in NBT-20KBT [18–21]. The electromechanical quality factor, Q_m, is in the range of 120–130 for NBT-xBT [12,22] and is 100 for NBT-xKBT [23] at the MPB. The properties of NBT-xBT can be modified by acceptor doping [12,24,25], changing the Bi or Na stoichiometry [26], forming a composite [27,28], precipitation hardening [29], or quenching [30–32]. Acceptor doping with Zn/Mg [33] or formation of a composite with ZnO are the most promising approaches [9] to improve the mechanical quality factor of NBT-xBT. In contrast, doping NBT-xKBT compositions has not yet been proven to affect Q_m. In PZT materials, mainly the acceptor doping approach is used to increase Q_m. [34,35].

NBT-xBT-based materials demonstrate a stable electromechanical quality factor as a function of vibration velocity, $Q_m(v)$, whereas Q_m experiences a sharp drop with increasing vibration velocity in PZT-based materials [36]. The stability of Q_m in the NBT-based materials is correlated to the low and velocity-independent extrinsic contributions [9]. It was evidenced that the trend in $Q_m(v)$ is similar across NBT-based materials, thus confirming it as an intrinsic material property.

However, the origin of the minor and velocity-independent extrinsic contributions has not been clarified as yet. To this end, the degree of poling-induced texture is quantified in this study in order to assess the domain wall motion under high-power drive. Then the correlation between remanent polarization and piezoelectric coefficient is ascertained to

*bremecker@ceramics.tu-darmstadt.de
†roedel@ceramics.tu-darmstadt.de

determine when the optimum poling degree has been reached. These data are correlated with the electromechanical quality factor. In order to have a complete picture with varying options to tune the NBT-based high-power piezoceramics, several material modifications are investigated. NBT-6BT is taken as the base material and contrasted to a Zn-doped NBT-6BT material, which has then been further quenched. NBT-6BT is also compared to a NBT-21KBT piezoceramic, which has been doped with Mg as a further acceptor option. All the materials are finally contrasted to a soft PZT material, which features extensive domain wall movement under electrical drive.

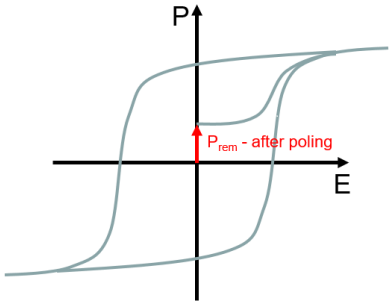

FIG. 1. Schematic of how to determine the remanent polarization of partial polarized samples.

II. EXPERIMENT

All NBT-based compositions were produced using the solid-state synthesis route. Exact compositions are $(1-x)Na_{1/2}Bi_{1/2}Ti_{(1-y)}Zn_yO_{3-x}BaTi_{(1-y)}Zn_yO_3$ with $x = 0.06$ and $y = 0$ for NBT-6BT, $x = 0.06$ and $y = 0.005$ for NBT-6BT-0.5Zn and $(1-x)Na_{1/2}Bi_{1/2}Ti_{(1-y)}Mg_yO_{3-x}K_{1/2}Bi_{1/2}Ti_{(1-y)}Mg_yO_3$ with $x = 0.21$ and $y = 0$ for NBT-21KBT, and $x = 0.21$ and $y = 0.005$ for NBT-21KBT-0.5Mg. The following starting raw materials were used (all Alfa Aesar GmbH & Co. KG, Germany): Na_2CO_3 (99.5%), $BaCO_3$ (99.8%), Bi_2O_3 (99.975%), TiO_2 (anatase with 99.6%), ZnO (99.99%), MgO (99.99%), and $KHCO_3$ (99.93%). After drying the powders for 24 h at 100 °C [$KHCO_3$ in vacuum at room temperature (RT)], the powders were weighed and milled in ethanol with yttria-stabilized zirconia balls for 24 h at 250 rpm in a planetary ball mill (Fritsch Pulverisette 5). Acceptor-doped compositions were milled for 6 h. Powders were dried and calcined afterwards at 900 °C for 3 h with a heating rate of 5 °C/min followed by a second milling and drying step.

The powder was then pressed into cylindrical samples with a diameter of 10–15 mm, first with a uniaxial pressure of about 40 MPa and afterwards with a hydrostatic pressure of 200–350 MPa. The sintering conditions were optimized for each composition to obtain high relative densities and maximized electromechanical properties. The same sintering conditions for all compositions resulted in not comparable densities, microstructure, and properties. Sintering of pure NBT-xBT compositions was conducted in an alumina crucible with the samples embedded in sacrificial powder of the same composition at 1150 °C for 3 h. NBT-21KBT was sintered at 1150 °C for 2 h and all acceptor-doped compositions at 1100 °C for 2 h. The heating rate for all compositions was 5 °C/min. Samples, which were cooled down in the furnace, are labeled "FC." If they were taken out of the furnace right after the sintering dwell time and quenched in air, then they are denoted as "Q" for quenched. The density was determined using the Archimedes principle. The grain sizes were quantified from scanning electron microscope (SEM) images (Philips XL30FEG, Amsterdam, Netherlands) on at least 150 grains. The samples were polished and thermally etched at 900 °C for 10 min before taking SEM images.

For electrical measurements, samples were ground from both sides to a thickness of 0.7–0.8 mm, which was followed by an annealing step at 400 °C for 60 min with 5 °C/min heating and cooling rate. Silver electrodes were sputtered onto the sample surfaces. Poling was performed by applying a dc field of 6 kV/mm for 15 min at RT for NBT-xBT-based compositions and 5 kV/mm for 10 min at 120 °C followed by field cooling with a cooling rate of 2 °C/min for NBT-xKBT-based compositions. With these poling conditions the highest piezoelectric activity was obtained. Small signal properties were determined with an impedance analyzer (Novocontrol Alpha-Analyzer, Montabaur, Germany) 24 h after poling according to European standard EN 50324-2 [37]. The direct piezoelectric coefficient was obtained with a Berlincourt d_{33} meter (Piezotest, PM300) 24 h after poling. Depolarization temperature was quantified from thermally stimulated depolarization current measurements (Keithley 6485). The remanent polarization as a function of electric poling field was measured using a Sawyer-Tower circuit. To establish the influence of the degree of poling, samples of each investigated composition were quantified with varying electric poling fields. Several complete loops were measured of the partial poled samples. Since the polarization of the loop is symmetric to the x axis, the polarization of the partial polarized samples can be correlated to the starting polarization of this measurement (Fig. 1).

Figure 2 provides a simplified schematic of the synchrotron measurement setup for obtaining the texturing degree of all compositions in the poled state. The diffraction experiments on the NBT-xBT-based samples were carried out at DESY (Hamburg, Germany) on Beamline P02.1 with an incident beam energy of ∼ 59.8 keV, which corresponds to a wavelength of 0.20718 Å. A two-dimensional (2D) 16-in. XRD 1621N ES Series PerkinElmer detector with a resolution of 2048 × 2048 pixels and a pixel size of 200 μm^2 was used to receive two-dimensional diffraction patterns. The beam center was placed in one corner of the detector to improve the angular resolution of the recorded patterns. For the NBT-xKBT samples, a different synchrotron setup was used at the ERSF in Grenoble with ∼60 keV beam energy (wavelength 0.20664 Å). The beam was centered onto a Pilatus3 X CdTe 2M detector.

The 2D patterns were integrated over 10° intervals to receive a one-dimensional (1D) XRD pattern representing a specific angular range Ψ in relation to the poling direction using DAWN software version 2.15.0 [38]. For example, the 1D pattern for $\Psi = 45°$ was obtained by integrating the 2D XRD pattern from 40° to 50°. For $\Psi = 2.5°$ and $\Psi = 87.5°$, data were integrated from 0° to 5° and from 85° to 90°, respectively. For materials with coexisting rhombohedral and

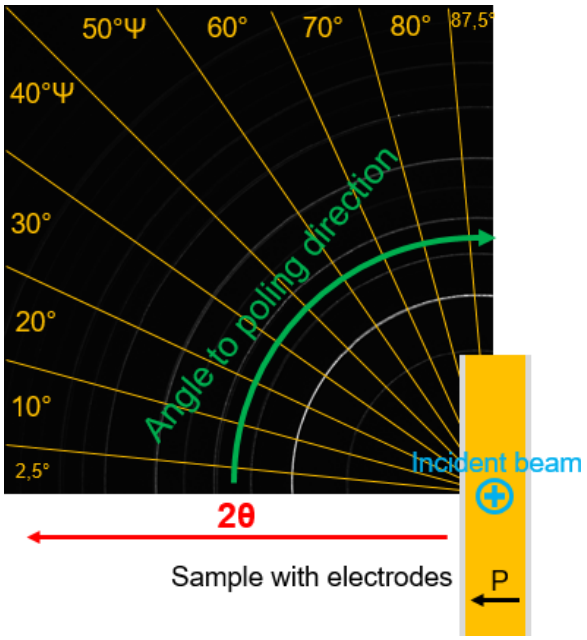

FIG. 2. Schematic sketch of the angle-dependent synchrotron measurement with the incident beam perpendicular to the poling direction of the sample.

tetragonal phases, the 111_{pc} and 200_{pc} reflections are each composed of three single peaks as exemplified in Fig. S1 in the Supplemental Material [39]. In the case of the 111_{pc} reflection, these are the two rhombohedral 111_R and $11\bar{1}_R$ and the tetragonal 111_T reflection, while the 200_{pc} reflection has contributions from the 200_R reflection of the rhombohedral phase and from the 002_T and 200_T reflections of the tetragonal phase. The 111_{pc} and 200_{pc} reflections of the extracted angle-dependent 1D diffraction patterns of the poled materials were each fitted with three peaks with pseudo-Voigt peak shape function to extract the integrated intensities for all fitted reflections. Based on the intensity ratios, texture factors were calculated for the rhombohedral and tetragonal phases by utilizing a weighted average of all orientations as in Ref. [40]. The angle-dependent integrated 1D patterns of the poled material were summed up with a weighting factor [Eq. (1)] with respect to the angle to the electric field to receive a refinable pattern with close to random texture [41]. Full pattern Rietveld refinements were carried out using TOPAS V6.

$$\langle I\rangle = \sum_{\propto=0^\circ}^{90^\circ} I(\propto)[\cos\ (\propto_i) - \cos(\propto_j)], \qquad (1)$$

with I = intensity and $\propto_i$ and $\propto_j$ as the low and high boundaries of the respective integrated angular bin.

Parts of the texture and strain analysis were performed using the STRAP (strain, texture and Rietveld analysis for piezoceramics [42]) method with the program package MAUD (materials analysis using diffraction) [43]. The lattice strain was refined with the WSODF (weighted strain orientation distribution function) model [44] and the texture was refined with the exponential harmonics model. During the Rietveld refinement, lattice parameters, scale factors, and microstructural parameters as well as atomic positions and Debye-Waller factors were treated. Details can be found elsewhere [42].

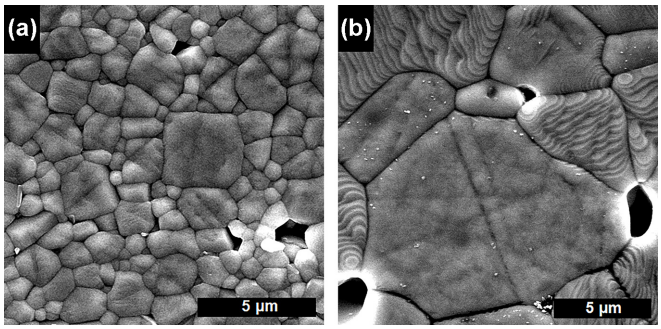

FIG. 3. SEM micrographs of NBT-6BT-FC (a) and NBT-6BT-0.5Zn-FC (b).

III. RESULTS AND DISCUSSION

A. Microstructure

All samples feature a relative density of 95%–97.3%. No secondary phases were detected in the x-ray diffraction patterns (Fig. S3 [39]). The grain size for pure NBT-6BT and NBT-21KBT is around 1–2 ± 0.8 µm. Zn doping significantly increases the grain size to about 10.4 ± 4.3 µm in NBT-6BT-0.5Zn-FC; see Fig. 3(b). The lower sintering temperature and time, as well as the larger grain size, suggest that Zn acts as a sintering aid. Mg doping does not alter the grain size of the NBT-21KBT (Fig. S2 [39]).

B. Electromechanical and structural characterization

Table I provides salient data for depolarization temperature T_d, planar electromechanical coupling factor Q_m^p, and longitudinal piezoelectric coefficient, d_{33}. Zn doping increases T_d and Q_m in agreement with the literature [12,22,45]. In this study, T_d of NBT-6BT is slightly higher with 111 °C as compared to 105 °C which was previously reported by us [22]. These small variations indicate sensitivity of the material to the processing route. Zn doping decreases d_{33} from 140 to 117 pC/N but results in an increase of Q_m of about 430%. Quenching of NBT-6BT-0.5Zn does not alter the mechanical loss considerably, but further increases T_d by 29 °C and decreases d_{33} slightly by 10 pC/N as compared to furnace-cooled Zn-doped NBT-6BT. This is in agreement with the literature in which a decrease of d_{33} of about 20 pC/N and an increase of T_d of about 26 °C were reported [22]. Quenching was not

TABLE I. Depolarization temperature T_d, planar mechanical quality factor Q_m^p, and piezoelectric constant d_{33} of all investigated lead-free compositions.

	T_d (°C)	Q_m^p	d_{33} (pC/N)
NBT-6BT	111	132 ± 11	140 ± 4
NBT-6BT-0.5Zn	142	570 ± 53	117 ± 3
NBT-6BT-0.5Zn-Q	173	516	107 ± 4
NBT-21KBT	114	72	170 ± 4
NBT-21KBT-0.5Mg	135	71 ± 20	154 ± 4

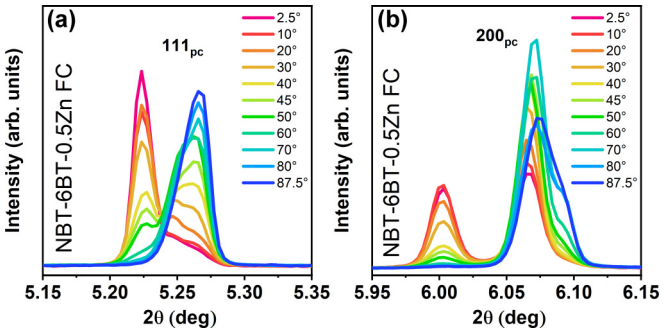

FIG. 4. X-ray diffraction profile of poled NBT-6BT-0.5Zn-FC for different azimuth angles: (a) 111_{pc} and (b) 200_{pc}.

investigated in the NBT-xKBT system. Doping NBT-21KBT with Mg leads to an increase in T_d, similar to the trend seen for the NBT-xBT system but to a smaller degree [33]. d_{33} decreases by 16 pC/N with Mg doping, but is higher in general for the NBT-xKBT system in comparison to the NBT-xBT system. Q_m is the same in both investigated NBT-21KBT compositions.

Rietveld refinement of data collected on poled samples revealed the constituent phases and lattice parameters of all compositions. All investigated compositions were refined using a phase mixture of rhombohedral *R*3*c* phase and tetragonal *P*4*mm* phase. This is in agreement with the literature for poled NBT-6BT and NBT-22KBT based on diffraction [46–49]. Pure NBT-6BT-FC consists of 84% *R*3*c* and 16% *P*4*mm*. NBT-6BT-0.5Zn-FC and NBT-6BT-0.5Zn-Q have a similar phase composition of about 75%–77% *R*3*c* and 23%–25% *P*4*mm*. This increase in tetragonal phase fraction was observed before in unpoled compositions and originates from a shift of the MPB of the NBT-xBT system [12]. A higher lattice distortion was observed in the NBT-6BT doped with Zn, in agreement with previous reports in the literature in which the lattice distortion was correlated to T_d [50]. Quenching additionally increases the lattice distortion in both the rhombohedral and tetragonal phase and further increases T_d. Doped and undoped NBT-21KBT exhibit similar phase fractions in the poled state of about 65% *R*3*c* and 35% *P*4*mm*. NBT-21KBT features an increased rhombohedral and tetragonal distortion upon doping with Mg. The increased lattice distortion is expected to have the same influence on T_d in the NBT-xKBT as in the NBT-xBT system. No influence of the phase composition and the degree of lattice distortion on Q_m could be established by comparing the structure and electromechanical properties.

C. Poling-induced remanent texture

Diffraction patterns feature the 111_{pc} and 200_{pc} reflections of NBT-6BT-0.5Zn-FC for different azimuthal angles in Fig. 4. The reflection intensities reveal an extreme dependence on azimuthal angle, indicating an enormous degree of remanent texture (diffraction patterns of other samples: see the Supplemental Material, Fig. S5 [39]). The 111_{pc} and 200_{pc} reflections of the investigated materials have contributions from coexisting rhombohedral and tetragonal phases. The reflections of both phases (R = rhombohedral and T = tetragonal) overlap partly due to the similarity in unit cell parameters. The intensity of the 111_R reflection strongly decreases with increasing azimuthal angle in the NBT-xBT compositions and vanishes at angles perpendicular to the direction of the poling field. The tetragonal 002_T vanishes in a similar fashion.

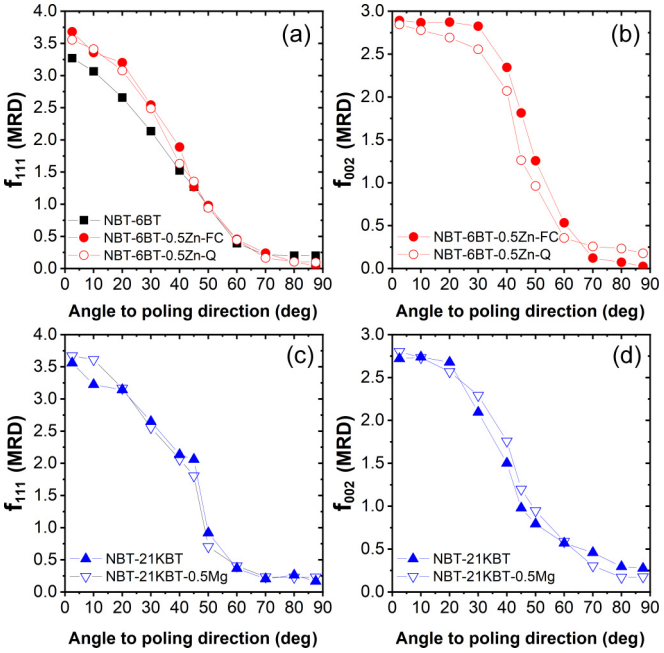

FIG. 5. Pole figure densities in multiples of random distribution, calculated with the standard method described by Jones *et al.* [50] for the rhombohedral *R*3*c* and tetragonal *P*4*mm* phase-based on the 111_{pc} and 200_{pc} sets of reflections, respectively, for NBT-6BT-FC, NBT-6BT-0.5Zn-FC, and NBT-6BT-0.5Zn-Q (a), (b) and for NBT-21KBT and NBT-21KBT-0.5Mg (c), (d).

D. Standard model to determine the texturing degree

Pole figure densities (PFDs) in MRD (multiples of random distribution) for the rhombohedral and tetragonal phases were calculated using the method described by Jones *et al.* [51]. The reference intensities were calculated by summing up the fitted intensities of all azimuthal angles with a weighting factor, similar to Eq. (1) [41]. The PFDs for all compositions are given in Fig. 5, except for the tetragonal phase of NBT-6BT-FC due to a strong reflection overlap of the $002_T/200_T$ doublet and the 200_R singlet leading to a large error. Still, the extreme texturing degree is qualitatively evident in the angle-dependent diffraction patterns (Fig. S5 [39]). All compositions exhibit a degree of texturing close to the theoretical maximum of the respective structural model (Fig. 5). The theoretical maximum for f_{111} of the rhombohedral phase is 4, while it is 3 for f_{002} of the tetragonal phase [51]. Due to the way the values are calculated, higher values are not possible for these symmetries. The theoretical minimum is 0 for both. Values close to the maximum and minimum are obtained at 2.5° and 87.5°, respectively. To set this into perspective: literature values are in the range of 1.2–1.5 MRD for PZT and $PbTiO_3$ (PT) and 2 MRD for $K_{0.5}Na_{0.5}NbO_3$ (KNN) [52,53]. Given are the PFDs for the tetragonal phase. The high texturing values in the NBT-based materials are believed to result

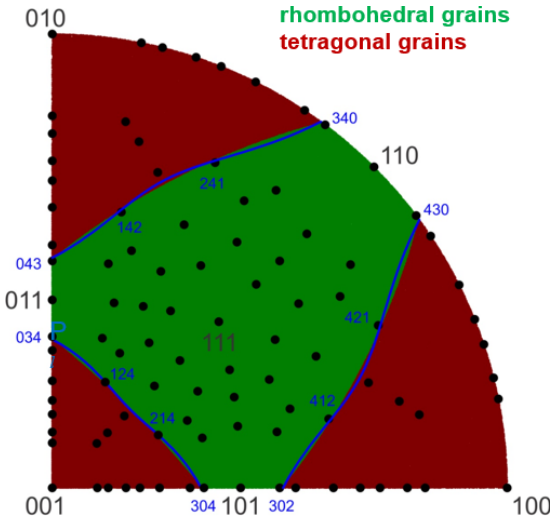

FIG. 6. Field-induced phase transformation into either a tetragonal or a rhombohedral phase, depending on the orientation of the randomly oriented grains to the field direction.

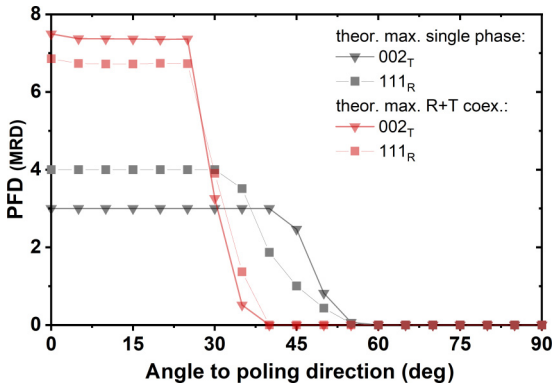

FIG. 7. Theoretical maximum PFDs in MRD for the tetragonal and rhombohedral phases in a single phase material in comparison to a two-phase material.

in the characteristic high-power properties. This correlation and the reason for the high texture are elaborated upon in the following sections.

E. Phase coexistence model to determine the texturing degree

The standard model poses limitations for a material with phase coexistence and phase transformation during the poling process. Therefore, a second model is introduced to calculate the texturing degree of the NBT-based materials presented here.

The orientation of a grain in relation to the poling field will influence the resulting crystal phase [45,54,55]. As a consequence, unit cells with a ⟨100⟩ axis closely aligned with the poling vector will preferably be transformed into a tetragonal phase. On the other hand, unit cells with a ⟨111⟩ axis closely aligned with the poling vector will preferably exhibit a rhombohedral distortion (Fig. 6). The exact boundaries are given by the blue lines in Fig. 6 (Eqs. (2)–(7) in the Supplemental Material [39]). If the field-induced distortion would only be dictated by the initial unit cell orientation, this would lead to a phase ratio of 57.1% rhombohedral and 42.9% tetragonal, since four out of seven possible polarization directions are rhombohedral. (rhombohedral = 4 equivalent polarization directions, tetragonal = 3 equivalent polarization directions, total polarization directions = 7. In 4/7 = 57.1% of the grains it transforms into rhombohedral and in 3/7 = 42.9% of the grains it transforms into tetragonal) [47,56]. However, the observed phase ratios (Table II) are shifted towards the rhombohedral side. It is most likely a result of chemical pressure since the abundance and quantity of certain ions on the A site strongly influence the symmetry and phase composition of a crystalline material.

Both the orientation-dependent phase transformation and the phase coexistence contribute to the extreme remanent texture found in the NBT-based materials. The three possible polarization directions of the tetragonal phase and the four directions of the rhombohedral phase add up in a multiphase system. The resulting theoretical maximum PFD is significantly higher than the values for single phase materials. Since phase coexistences are exceptionally important for high properties [57], this scenario is of paramount relevance for potential applications. In the case of coexisting tetragonal and rhombohedral phases, the theoretical limit of the PFD is slightly above 7 MRD for the tetragonal phase and almost 7 MRD in the rhombohedral phase (Fig. 7). The PFD can be used to calculate the maximum achievable polarization in relation to the spontaneous polarization, according to the model described in Ref. [58]. The maximum polarization of 93% and 92.6% for the tetragonal and rhombohedral phase can be achieved when taking two coexisting phases into account. In

TABLE II. Structural characteristics obtained from Rietveld refinement (poled samples). The error is smaller than the last digit. The x-ray profile and the fitted curves are given in Fig. S4 [39]. Tetragonal lattice distortion = $c_{tet}/a_{tet}-1$. Rhombohedral lattice distortion = $90^\circ-\alpha_{rhom}$. For the calculation of the rhombohedral lattice distortion the hexagonal unit cell parameters are converted into rhombohedral unit cell parameters.

NBT-6BT	$R3c$(%)	$P4mm$(%)	a_{rhom}(Å)	c_{rhom}(Å)	a_{tet}(Å)	c_{tet}(Å)	90-α_{rhom}	$c/a-1$ (%)	R_{wp}(%)
Pure-FC	84	16	5.510	13.607	3.894	3.943	0.312	1.26	3.35
0.5Zn-FC	75	25	5.502	13.593	3.888	3.944	0.328	1.42	4.30
0.5Zn-Q	77	23	5.501	13.599	3.887	3.948	0.352	1.58	3.02
NBT-21KBT-									
Pure-FC	63	37	5.509	13.583	3.891	3.939	0.251	1.23	4.85
0.5Mg-FC	65	35	5.509	13.590	3.891	3.943	0.271	1.34	4.79

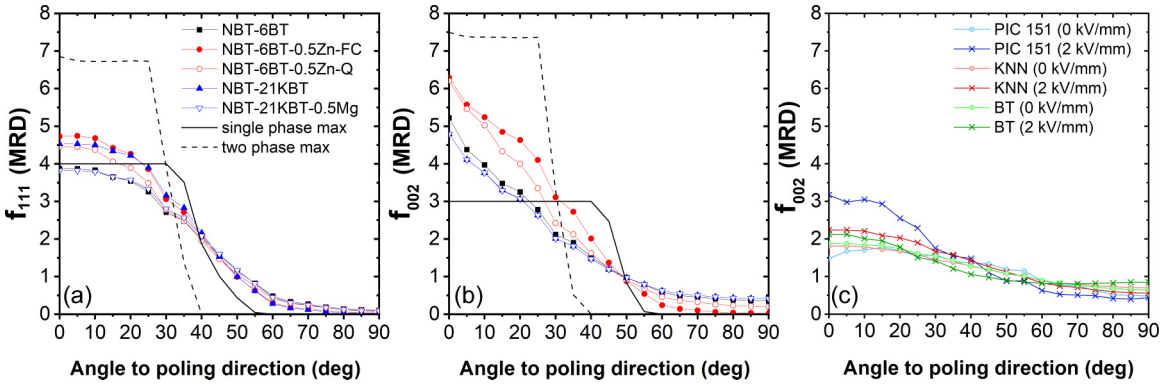

FIG. 8. PFDs in MRD, calculated with the STRAP method described by Hinterstein *et al.* [42,59]: (a) rhombohedral and (b) tetragonal texturing factors of NBT-6BT, NBT-6BT-0.5Zn-FC, NBT-6BT-0.5Zn-Q; NBT-21KBT, and NBT-21KBT-0.5Mg; (c) tetragonal texturing factors at 0 and 2 kV/mm of soft PZT (PIC151), BT, and KNN.

a single phase polycrystalline material, the maximum achievable polarization is 83.1% and 86.6% in comparison.

The effect of phase coexistence on the measured PFD was evaluated by using the STRAP model. The STRAP model (strain, texture, and Rietveld analysis for piezoceramics) accounts for the tetragonal and rhombohedral phase coexistence, allows one to use the full diffraction data from all angles simultaneously, and uses a structure model to extract the strain and texture values in a combined refinement approach [42,59]. The STRAP method results in a smaller error in comparison to the standard model since the information from the complete diffraction pattern is used instead of fitting only the 111_{pc} and 200_{pc} sets of reflections. Relatively high PFD values were obtained using the STRAP model [Figs. 8(a) and 8(b)], especially in comparison to PZT, PT, KNN, and BT ($BaTiO_3$)[1] with values around 2 without electric field [Fig. 8(c)] [43,52,53,60]. *In situ* measurements at 2 kV/mm revealed a considerable increase in the texturing degree of soft PZT and KNN but just a minor increase in BT. Most important to note, even at 2 kV/mm the texturing degrees are much lower in the non-NBT-based materials in comparison to the NBT-based materials at zero field.

Both methods to determine the PFD exhibit the same trend. In the tetragonal phase an increased degree of texture in NBT-6BT-0.5Zn-FC is observed in comparison to the undoped material. Zn doping NBT-*x*BT shifts the phase fraction towards the 57/43 ratio. It is likely that the rhombohedral and tetragonal phases become energetically more equivalent, leading to more unit cell orientation-dependent phase stability and therefore to a higher texturing degree as seen. The PFD of NBT-6BT-0.5Zn-Q is marginally smaller in comparison to NBT-6BT-0.5Zn-FC. NBT-21KBT-based compositions exhibit the same degree of texture regardless of being doped with Mg or undoped. The rhombohedral phase is also highly textured in all compositions with values of roughly 4–5 MRD close to the electric field direction. The same tendencies as for the tetragonal phase are present except for the pure NBT-21KBT. When using the STRAP method, it has a slightly larger PFD value as compared to NBT-21KBT-0.5Mg. The reason for that is unknown.

Figure 9 schematically depicts two different materials. The NBT-based material represents a material with high remanent texture and a commercially soft lead zirconate titanate (PZT), PIC151 (PI ceramics, Lederhose, Germany), represents a material with lower remanent texture. Although the soft PZT has a rhombohedral and tetragonal phase mixture, the remanent texture is within the limits of the single phase theory. Both materials have the same random distribution of polar vectors in the unpoled state, Fig. 9(a). However, in contrast to NBT-based materials, PZT already features a coexistence of distorted phases in the unpoled state. After poling, in the remanent state, soft PZT has a smaller degree of remanent texture in comparison to the NBT-based materials, Fig. 9(b). The application of an external electric field will lead to further alignment of polar vectors. The difference of the remanent state and during the application of an electric field is larger in soft PZT in comparison to NBT-based materials, Fig. 9(c). Jones *et al.* [51,52] discussed the proportionality of domain switching contributions and degree of texture in the context of the poling process. The possibility and probability of reorientation is decreasing from a certain threshold of texturing degree. In other words, when a certain degree of poling-induced texture is exceeded, the extrinsic contributions during small-signal application will decrease upon further increase of poling-induced texture.

Theoretically, in a perfectly textured material, the extrinsic contributions are zero, e.g., in a monodomain single crystal. In general, the piezoelectric response is generated by intrinsic contributions and extrinsic contributions [57,61]. The intrinsic contributions are divided into polarization extension and rotation. Depending on the contribution from rotation and extension, the perfect angle for the highest intrinsic contributions can be calculated. NBT-based materials are classified as extenders and have the highest intrinsic contributions parallel to the polarization direction [62,63]. The extrinsic contributions are attributed to domain wall movement and, therefore, domain switching strain. Domains with orientation close to the external field direction grow when applying an external force like an electric field. Hinterstein *et al.* [42] investigated the texturing of soft PZT (PIC151) in the remanent state and *in situ* with an electric field amplitude of 2 kV/mm. The

[1]These data cannot be found as given in Fig. 8(c) in the listed publications but were kindly shared with us by the authors.

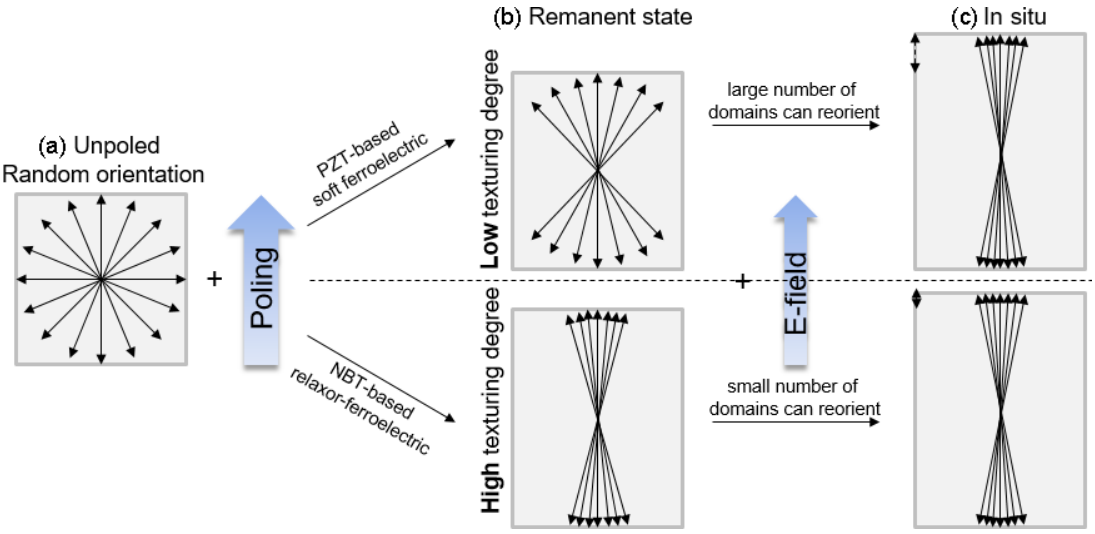

FIG. 9. Schematic pole figures of the extrinsic contributions for a low-textured material and a high-textured material after poling.

soft PZT exhibits a considerable reversibility in the texturing degree between the remanent and *in situ* state due to the significant back-switching of domains.

In general, the extrinsic contributions are composed of the degree of domain reorientation and the amplitude of spontaneous strain [42,51]. In NBT-based materials the orientation along the field direction after poling is close to the theoretical maximum. The degree of orientation cannot increase significantly anymore. This is confirmed by Hinterstein *et al.* [47]. They unveiled just a minor reversibility in the 111_{pc} and 200_{pc} reflections of NBT-6BT in the remanent and at the *in situ* state (4 kV/mm). Additionally, the lattice distortion is higher in the rhombohedral phase of the lead-free materials with around 0.86%–0.93% in comparison to 0.5% in PIC151 [42]. The tetragonal lattice distortions of both material systems are comparable. Hence, the amplitude of spontaneous strain is higher in the lead-free material. A higher amplitude of spontaneous strain results in fewer switching processes for the same amount of total strain. Fewer switching processes correlate to smaller loss.

The *in situ* electric-field-induced texturing degree of NBT-6BT was evaluated before by Wohninsland *et al.* [64]. A considerably smaller change in the reflection intensities as a function of azimuthal angle was apparent due to an inferior 2θ resolution compared to this study, resulting in a smaller calculated degree of texturing reported.

IV. IMPACT ON PIEZOELECTRIC COEFFICIENT

The piezoelectric coefficient d_{33} comprises intrinsic and extrinsic contributions. The intrinsic contributions in NBT-based materials are assumed to increase linearly with increasing degree of poling. In contrast, the extrinsic contributions, above a certain threshold, may even decrease with increasing poling degree, respectively, remanent polarization. This effect was probed for different NBT-based piezoceramics and contrasted to soft PZT in Fig. 10, highlighting the piezoelectric constant d_{33} as a function of remanent polarization, P_{rem}. d_{33} of the reference soft PZT increases linearly with increasing poling degree [Fig. 10(a)]. Hence, the soft PZT is still in the linear regime, as expected from the comparably small texturing degree reported in the literature [42]. In contrast, d_{33} deviates from the linear relationship with remanent polarization for all NBT-based materials at polarization levels between 20 and 30 $\mu C/cm^2$. For the NBT-BT-based materials, the piezoelectric constant appears to saturate and decreases for the case of the NBT-6BT-0.5Zn-FC. For the directly comparable NBT-6BT variants, this behavior reflects the differences in poling textures, Fig. 8. The Zn-doped material features higher poling texture and therefore reaches the maximum piezoelectric coefficient before the maximum remanent polarization is obtained.

When assuming a linear intrinsic contribution and subtracting the overall piezoelectric response, the extrinsic contributions can be separated in Fig. 10(c). We considered an extrinsic contribution of about 5% for NBT-6BT in the fully poled state as evaluated by Slabki *et al.* [9]. The extrinsic contribution clearly reveals a decreasing trend at larger P_{rem}. This reduced piezoelectric activity is suggested to be related to a reduced domain wall (DW) density due to the higher degree of texturing.

V. FERROELECTRIC HARDENING MECHANISM

Recently, NBT-xBT materials were classified as having minor extrinsic contributions to the overall strain in resonance [9]. In addition, the extrinsic contributions do not increase with increasing vibration velocity, thereby yielding a stable mechanical quality factor Q_m with vibration velocity [9]. The reason for the absence of larger extrinsic contributions has been still unclear. Here, it was established that the extreme poling-induced texturing degree directly correlates with minor extrinsic contributions. Therefore, the ferroelectric hardening mechanism in NBT-based compositions is believed to differ from the established hardening mechanism in PZT-based materials. In PZT (and BT), acceptor doping leads to the formation of defect dipoles which restrict domain wall motion (Fig. 11). The hardening takes place after poling by diffusion of oxygen vacancies and alignment of the defect couples [65–67]. In NBT-based materials, space charges are important

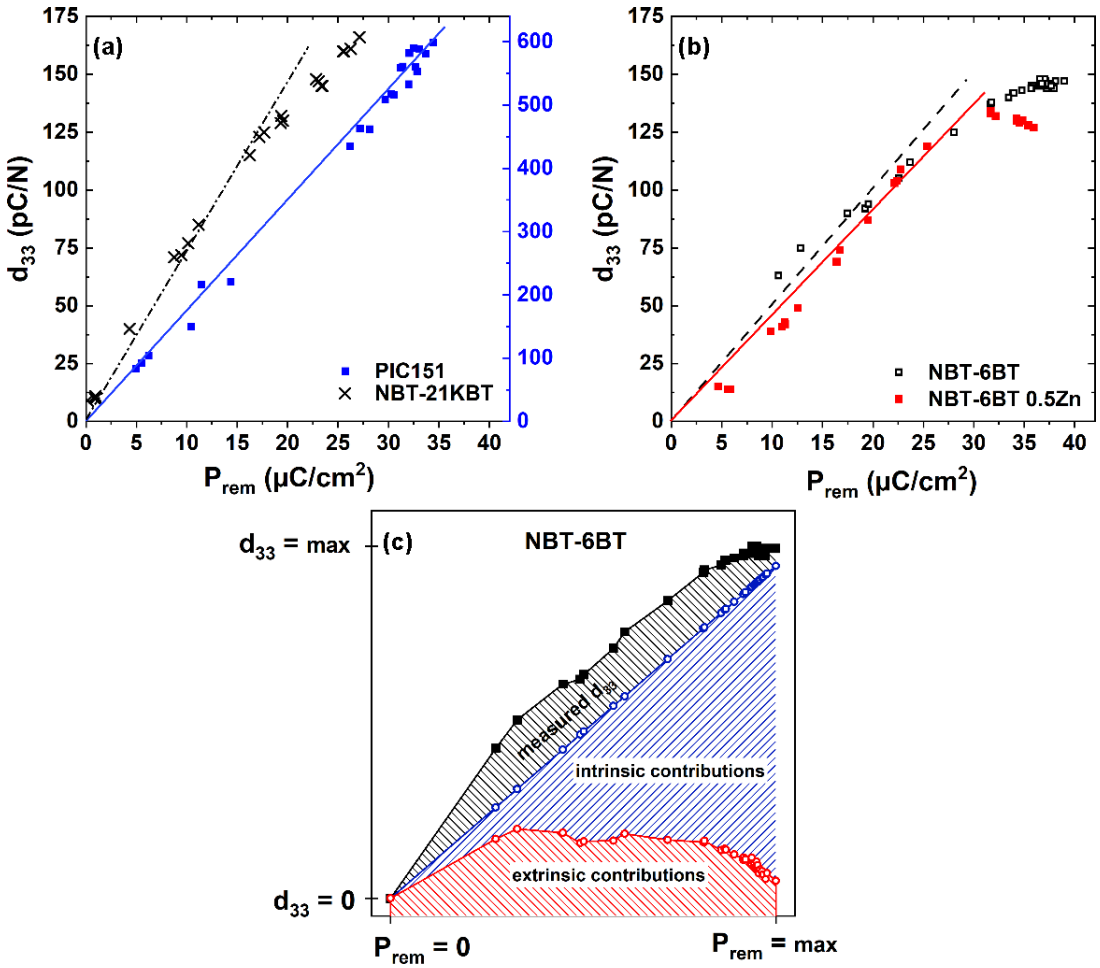

FIG. 10. Remanent polarization P_{rem} against the piezoelectric coefficient d_{33} for (a) NBT-21KBT, soft PZT, and (b) NBT-6BT, NBT-6BT-0.5Zn. (c) Intrinsic and extrinsic contribution to the overall d_{33} in NBT-6BT with different remanent polarization P_{rem} (equivalent to poling degree).

for ferroelectric hardening rather than defect dipoles [33]. Domains are highly aligned during the poling process. The margin for further alignment diminishes, hence reducing domain wall movement (Fig. 11).

In ferroelectric hardened NBT, the movement of individual domain walls is not affected but rather the number/volume of domains which are able to align is reduced. This results in a reduced domain wall density. When the degree of texture is close to saturation (Fig. 8), as is the case with lead-free materials in this study, even a strong driving force like an extreme vibration velocity cannot induce much domain wall motion [9]. Thus, extrinsic contributions are limited. In the literature the correlation between domain wall density, domain wall mobility, and the piezoelectric response is discussed too. Lemos da Silva *et al.* [60] and Picht *et al.* [68] found the highest piezoelectric response at a grain size of about 1 μm in BT and PZT, respectively. The domain wall density and domain wall mobility are interrelated phenomena. Both depend on the

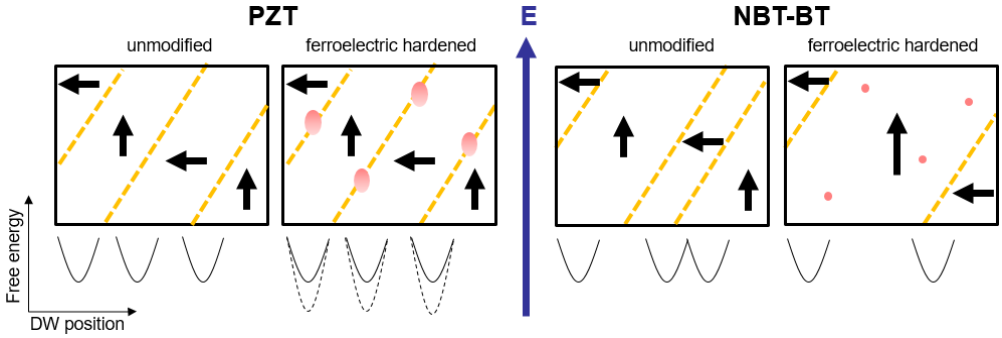

FIG. 11. Comparison of domain alignment and corresponding free-energy profile before and after ferroelectric hardening in PZT and NBT-BT.

grain size, resulting in an optimized grain size for a maximum piezoelectric response. Li *et al.* [69] additionally revealed the effect of the domain wall density on the mechanical loss.

Extrinsic contributions are the main reason for heat production in high-power applications [9]. Therefore, our hypothesis is that the high degree of poling-induced texture is a major reason for the excellent high-power properties of the NBT-based materials. Furthermore, acceptor doping increases the remanent texture and Q_m in NBT-6BT but not in NBT-21KBT. Quenching changes neither the texturing degree nor Q_m. The degree of texture hence appears related to Q_m in the NBT-based materials. It should be noted that the statement "higher texturing degree leads to a higher Q_m" does not apply in all circumstances, but only if the degree of texture surpasses a certain threshold where the extrinsic contributions diminish.

VI. CONCLUSIONS

NBT-based materials exhibit extremely high remanent poling-induced texture which is stable towards high vibration velocity. This behavior has been corroborated with measurements correlating the piezoelectric constant, d_{33}, as a function of remanent polarization. Here, a maximum in piezoelectric coefficient at intermediate remanent polarization signifies a maximum in extrinsic contributions to d_{33}. Furthermore, the degree of texture correlates with the mechanical quality factor. It indicates a ferroelectric hardening mechanism in which the texturing degree plays an important role for ferroelectric hardening in NBT-based materials. This concept might be applicable to other material systems too. It differs from the classical defect dipole concept known from PZT and BT and hence extends the tools for ferroelectric hardening. The concept provides a more detailed explanation of the unique high-power properties of NBT-based materials which are seen as a promising replacement for PZT in high-power applications [70].

ACKNOWLEDGMENTS

Daniel Bremecker, Siegfried Teuber, and Jürgen Rödel gratefully acknowledge financial support by the Bundesministerium für Bildung und Forschung (Project No. 13XP5091B). L.K.V. and A.W. thank the Deutsche Forschungsgemeinschaft (DFG) for financial support under Proposals No. KO 5948/1-1 and No. KL 615/34-1 (Grant No. 414311761) and DESY (Proposal No. I-20200532). M.H. thanks the Deutsche Forschungsgemeinschaft (DFG) under Grant No. HI1867/1-2 and the Fraunhofer Internal Program under Grant No. Attract 40-04857 for financial support. The authors acknowledge DESY (Hamburg, Germany), a member of the Helmholtz Association HGF, for the provision of experimental facilities. Parts of this research were carried out at beamline P02.1. Beam time was allocated for Proposals No. I-20191018, No. I-20200532, and No. I-20210624.

No conflict of interest exists in the submission of this paper. The manuscript is approved by all authors for publication.

[1] A. J. Bell and O. Deubzer, Lead-free piezoelectrics—The environmental and regulatory issues, MRS Bull. **43**, 581 (2018).

[2] J.-F. Li, *Lead-Free Piezoelectric Materials* (John Wiley & Sons, New York, 2020).

[3] J. Rödel, K. G. Webber, R. Dittmer, W. Jo, M. Kimura, and D. Damjanovic, Transferring lead-free piezoelectric ceramics into application, J. Eur. Ceram. Soc. **35**, 1659 (2015).

[4] T. N. Nguyen, H.-C. Thong, Z.-X. Zhu, J.-K. Nie, Y.-X. Liu, Z. Xu, P.-S. Soon, W. Gong, and K. Wang, Hardening effect in lead-free piezoelectric ceramics, J. Mater. Res. **36**, 996 (2021).

[5] M. Gagliardi, Lead-free piezoelectric ceramics: Technologies and global opportunities, BCC Research Report No. NAN063A (2019).

[6] S. I. Shkuratov and C. S. Lynch, A review of ferroelectric materials for high power devices, J. Materiomics **8**, 739 (2022).

[7] H. N. Shekhani, E. A. Gurdal, S. O. Ural, and K. Uchino, Analysis of high power behavior in piezoelectric ceramics from a mechanical energy density perspective, arXiv:1605.06685.

[8] S. Zhang, H. J. Lee, and T. R. Shrout, U.S. Patent No. 8,501,031. Washington, DC: U.S. Patent and Trademark Office, (2013).

[9] M. Slabki, K. V. Lalitha, J. Rödel, and J. Koruza, Origin of high-power drive stability in $(Na_{1/2}Bi_{1/2})TiO_3$-$BaTiO_3$ based piezoceramics, Acta Mater. **227**, 117703 (2022).

[10] T. Takenaka, K.-i. Maruyama, and K. Sakata, $(Bi_{1/2}Na_{1/2})TiO_3$-$BaTiO_3$ system for lead-free piezoelectric ceramics, Jpn. J. Appl. Phys. **30**, 2236 (1991).

[11] O. Elkechai, M. Manier, and J. P. Mercurio, $Na_{0.5}Bi_{0.5}TiO_3$-$K_{0.5}Bi_{0.5}TiO_3$ (NBT-KBT) system: A structural and electrical study, Phys. Status Solidi A **157**, 499 (1996).

[12] D. Bremecker, K. Lalitha, S. Teuber, J. Koruza, and J. Rödel, Influence of Zn^{2+} doping on the morphotropic phase boundary in lead-free piezoelectric $(1-x)$ $Na_{1/2}Bi_{1/2}TiO_3$-$x$$BaTiO_3$, J. Am. Ceram. Soc. **105**, 1232 (2021).

[13] Y. Hiruma, K. Yoshii, H. Nagata, and T. Takenaka, Phase transition temperature and electrical properties of $(Bi_{1/2}Na_{1/2})TiO_3$-$(Bi_{1/2}A_{1/2})TiO_3$ (A = Li and K) lead-free ferroelectric ceramics, J. Appl. Phys. **103**, 084121 (2008).

[14] M. Otoničar, S. Škapin, M. Spreitzer, and D. Suvorov, Compositional range and electrical properties of the morphotropic phase boundary in the $Na_{0.5}Bi_{0.5}TiO_3$-$K_{0.5}Bi_{0.5}TiO_3$ system, J. Eur. Ceram. Soc. **30**, 971 (2010).

[15] Y. R. Zhang, J. F. Li, and B. P. Zhang, Enhancing electrical properties in NBT–KBT lead-free piezoelectric ceramics by optimizing sintering temperature, J. Am. Ceram. Soc. **91**, 2716 (2008).

[16] R. Dittmer, W. Jo, E. Aulbach, T. Granzow, and J. Rodel, Frequency-dependence of large-signal properties in lead-free piezoceramics, J. Appl. Phys. **112**, 014101 (2012).

[17] F. H. Schader, Z. Y. Wang, M. Hinterstein, J. E. Daniels, and K. G. Webber, Stress-modulated relaxor-to-ferroelectric transition in lead-free $(Na_{1/2}Bi_{1/2})$ TiO_3-$BaTiO_3$ ferroelectrics, Phys. Rev. B **93**, 134111 (2016).

[18] G. D. Adhikary, D. Sharma, P. Punetha, G. Jafo, G. Abebe, A. Mishra, A. Senyshyn, and R. Ranjan, Preponderant influence

of disordered *P*4*bm* phase on the piezoelectricity of critical compositions of $Na_{0.5}Bi_{0.5}TiO_3$-based ferroelectrics, Phys. Rev. B **104**, 184102 (2021).

[19] Y. Hiruma, K. Yoshii, H. Nagata, and T. Takenaka, Investigation of phase transition temperatures on $(Bi_{1/2}Na_{1/2})TiO_3$-$(Bi_{1/2}K_{1/2})TiO_3$ and $(Bi_{1/2}Na_{1/2})TiO_3$-$BaTiO_3$ lead-free piezoelectric ceramics by electrical measurements, Ferroelectrics **346**, 114 (2007).

[20] K. Yoshii, Y. Hiruma, H. Nagata, and T. Takenaka, Electrical properties and depolarization temperature of $(Bi_{1/2}Na_{1/2})TiO_3$-$(Bi_{1/2}K_{1/2})TiO_3$ lead-free piezoelectric ceramics, Jpn. J. Appl. Phys. **45**, 4493 (2006).

[21] F. Weyland, M. Acosta, M. Vögler, Y. Ehara, J. Rödel, and N. Novak, Electric field–temperature phase diagram of sodium bismuth titanate-based relaxor ferroelectrics, J. Mater. Sci. **53**, 9393 (2018).

[22] L. Kodumudi Venkataraman, T. Zhu, M. P. Salazar, K. Hofmann, A. I. Waidha, J. Jaud, P. B. Groszewicz, and J. Rödel, Thermal depolarization and electromechanical hardening in Zn^{2+}-doped $Na_{1/2}Bi_{1/2}TiO_3$-$BaTiO_3$, J. Am. Ceram. Soc. **104**, 2201 (2020).

[23] A. Sasaki, T. Chiba, Y. Mamiya, and E. Otsuki, Dielectric and piezoelectric properties of $(Bi_{0.5}Na_{0.5})TiO_3$–$(Bi_{0.5}K_{0.5})TiO_3$ systems, Jpn. J. Appl. Phys. **38**, 5564 (1999).

[24] Q. Xu, M. Chen, W. Chen, H.-X. Liu, B.-H. Kim, and B.-K. Ahn, Effect of CoO additive on structure and electrical properties of $(Na_{0.5}Bi_{0.5})0.93\,Ba_{0.07}TiO_3$ ceramics prepared by the citrate method, Acta Mater. **56**, 642 (2008).

[25] E. Sapper, R. Dittmer, D. Damjanovic, E. Erdem, D. J. Keeble, W. Jo, T. Granzow, and J. Rödel, Aging in the relaxor and ferroelectric state of Fe-doped $(1–x)(Bi_{1/2}Na_{1/2})TiO_3$-$xBaTiO_3$ piezoelectric ceramics, J. Appl. Phys. **116**, 104102 (2014).

[26] S. Prasertpalichat and D. P. Cann, Hardening in non-stoichiometric $(1-x)Bi_{0.5}Na_{0.5}TiO_3$-$xBaTiO_3$ lead-free piezoelectric ceramics, J. Mater. Sci. **51**, 476 (2015).

[27] J. Zhang, Z. Pan, F.-F. Guo, W.-C. Liu, H. Ning, Y. Chen, M.-H. Lu, B. Yang, J. Chen, and S.-T. Zhang, Semiconductor/relaxor 0–3 type composites without thermal depolarization in $Bi_{0.5}Na_{0.5}TiO_3$-based lead-free piezoceramics, Nat. Commun. **6**, 6615 (2015).

[28] L. K. V., L. M. Riemer, J. Koruza, and J. Rödel, Hardening of electromechanical properties in piezoceramics using a composite approach, Appl. Phys. Lett. **111**, 022905 (2017).

[29] C. Zhao, S. Gao, T. Yang, M. Scherer, J. Schultheiß, D. Meier, X. Tan, H. J. Kleebe, L. Q. Chen, and J. Koruza, Precipitation hardening in ferroelectric ceramics, Adv. Mater. **33**, 2102421 (2021).

[30] T. Miura, H. Nagata, and T. Takenaka, Quenching effects on piezoelectric properties and depolarization temperatures of $(Bi_{0.5}Na_{0.5})TiO_3$-based solid solution systems, Jpn. J. Appl. Phys. **56**, 10PD05 (2017).

[31] L. KV, J. Koruza, and J. Rödel, Propensity for spontaneous relaxor-ferroelectric transition in quenched $(Na_{1/2}Bi_{1/2})TiO_3$-$BaTiO_3$ compositions, Appl. Phys. Lett. **113**, 252902 (2018).

[32] H. Muramatsu, H. Nagata, and T. Takenaka, Quenching effects for piezoelectric properties on lead-free $(Bi_{1/2}Na_{1/2})TiO_3$ ceramics, Jpn. J. Appl. Phys. **55**, 10TB07 (2016).

[33] D. Bremecker, M. Slabki, J. Koruza, and J. Rödel, Characterization of crystal structure, electrical and electromechanical properties of Mg-doped $0.94\,Na_{1/2}Bi_{1/2}TiO_3$-$0.06\,BaTiO_3$, J. Eur. Ceram. Soc. **42**, 5591 (2022).

[34] H. Dederichs and G. Arlt, Aging of Fe-doped PZT ceramics and the domain wall contribution to the dielectric constant, Ferroelectrics **68**, 281 (1986).

[35] U. Robels and G. Arlt, Domain wall clamping in ferroelectrics by orientation of defects, J. Appl. Phys. **73**, 3454 (1993).

[36] M. Slabki, L. K. Venkataraman, S. Checchia, L. Fulanović, J. Daniels, and J. Koruza, Direct observation of domain wall motion and lattice strain dynamics in ferroelectrics under high-power resonance, Phys. Rev. B **103**, 174113 (2021).

[37] European Standards, Piezoelectric properties of ceramic materials and components—Part 2: Methods of measurement–Low power, BS EN 50324-2 (2002).

[38] J. Filik, A. W. Ashton, P. C. Y. Chang, P. A. Chater, S. J. Day, M. Drakopoulos, M. W. Gerring, M. L. Hart, O. V. Magdysyuk, S. Michalik, A. Smith, C. C. Tang, N. J. Terrill, M. T. Wharmby, and H. Wilhelm, Processing two-dimensional x-ray diffraction and small-angle scattering data in DAWN 2, J. Appl. Crystallogr. **50**, 959 (2017).

[39] See Supplemental Material at http://link.aps.org/supplemental/10.1103/PhysRevMaterials.7.064407 for exture-based ferroelectric hardening in $Na_{1/2}Bi_{1/2}TiO_3$-based piezoceramics such as microstructure, XRD pattern or TSDC measurements.

[40] J. E. Daniels, W. Jo, J. Rödel, and J. L. Jones, Electric-field-induced phase transformation at a lead-free morphotropic phase boundary: Case study in a $93\%(Bi_{0.5}Na_{0.5})TiO_3$-$7\%$ $BaTiO_3$ piezoelectric ceramic, Appl. Phys. Lett. **95**, 032904 (2009).

[41] J. E. Daniels, W. Jo, J. Rodel, V. Honkimaki, and J. L. Jones, Electric-field-induced phase-change behavior in $(Bi_{0.5}Na_{0.5})TiO_3$-$BaTiO_3$-$(K_{0.5}Na_{0.5})NbO_3$: A combinatorial investigation, Acta Mater. **58**, 2103 (2010).

[42] M. Hinterstein, M. Hoelzel, J. Rouquette, J. Haines, J. Glaum, H. Kungl, and M. Hoffman, Interplay of strain mechanisms in morphotropic piezoceramics, Acta Mater. **94**, 319 (2015).

[43] J. Grässlin, L. B. McCusker, C. Baerlocher, F. Gozzo, B. Schmitt, and L. Lutterotti, Advances in exploiting preferred orientation in the structure analysis of polycrystalline materials, J. Appl. Crystallogr. **46**, 173 (2013).

[44] N. C. Popa and D. Balzar, Elastic strain and stress determination by Rietveld refinement: Generalized treatment for textured polycrystals for all Laue classes, J. Appl. Crystallogr. **34**, 187 (2001).

[45] L. Li, M. Zhu, K. Zhou, Q. Wei, M. Zheng, and Y. Hou, Delayed thermal depolarization of $Bi_{0.5}Na_{0.5}TiO_3$-$BaTiO_3$ by doping acceptor Zn^{2+} with large ionic polarizability, J. Appl. Phys. **122**, 204104 (2017).

[46] N. H. Khansur, M. Hinterstein, Z. Y. Wang, C. Groh, W. Jo, and J. E. Daniels, Electric-field-induced strain contributions in morphotropic phase boundary composition of $(Bi_{1/2}Na_{1/2})TiO_3$-$BaTiO_3$ during poling, Appl. Phys. Lett. **107**, 242902 (2015).

[47] M. Hinterstein, L. Schmitt, M. Hoelzel, W. Jo, J. Rödel, H.-J. Kleebe, and M. Hoffman, Cyclic electric field response of morphotropic $Bi_{1/2}Na_{1/2}TiO_3$-$BaTiO_3$ piezoceramics, Appl. Phys. Lett. **106**, 222904 (2015).

[48] R. Garg, B. N. Rao, A. Senyshyn, P. S. R. Krishna, and R. Ranjan, Lead-free piezoelectric system $(Na_{0.5}Bi_{0.5})TiO_3$-$BaTiO_3$: Equilibrium structures and

irreversible structural transformations driven by electric field and mechanical impact, Phys. Rev. B **88**, 014103 (2013).

[49] G. D. Adhikary, D. K. Khatua, A. Senyshyn, and R. Ranjan, Random lattice strain and its relaxation towards the morphotropic phase boundary of $Na_{0.5}Bi_{0.5}TiO_3$-based piezoelectrics: Impact on the structural and ferroelectric properties, Phys. Rev. B **99**, 174112 (2019).

[50] H. Luo, H. Liu, S. Deng, S. Hu, L. Wang, B. Gao, S. Sun, Y. Ren, L. Qiao, and J. Chen, Simultaneously enhancing piezoelectric performance and thermal depolarization in lead-free (Bi, Na)TiO_3-$BaTiO_3$ via introducing oxygen-defect perovskites, Acta Mater. **208**, 116711 (2021).

[51] J. L. Jones, M. Hoffman, and K. J. Bowman, Saturated domain switching textures and strains in ferroelastic ceramics, J. Appl. Phys. **98**, 024115 (2005).

[52] J. L. Jones, B. J. Iverson, and K. J. Bowman, Texture and anisotropy of polycrystalline piezoelectrics, J. Am. Ceram. Soc. **90**, 2297 (2007).

[53] B. Liu, P. Li, B. Shen, J. Zhai, Y. Zhang, F. Li, and X. Liu, Simultaneously enhanced piezoelectric response and piezoelectric voltage coefficient in textured KNN-based ceramics, J. Am. Ceram. Soc. **101**, 265 (2018).

[54] G. Esteves, C. M. Fancher, S. Röhrig, G. A. Maier, J. L. Jones, and M. Deluca, Electric-field-induced structural changes in multilayer piezoelectric actuators during electrical and mechanical loading, Acta Mater. **132**, 96 (2017).

[55] T. Nishikubo, T. Ogata, L. K. Venkataraman, D. Isaia, Z. Pan, Y. Sakai, L. Hu, S. Kawaguchi, A. Machida, and T. Watanuki, Polarization-and strain-mediated control of negative thermal expansion and ferroelasticity in $BiInO_3$-$BiZn_{1/2}Ti_{1/2}O_3$, Chem. Mater. **33**, 1498 (2021).

[56] J. Zhao, S. D. Funni, E. R. Molina, E. C. Dickey, and J. L. Jones, Orientation-dependent, field-induced phase transitions in soft lead zirconate titanate piezoceramics, J. Eur. Ceram. Soc. **41**, 3357 (2021).

[57] D. Damjanovic, Contributions to the piezoelectric effect in ferroelectric single crystals and ceramics, J. Am. Ceram. Soc. **88**, 2663 (2005).

[58] J. L. Jones, The effect of crystal symmetry on the maximum polarization of polycrystalline ferroelectric materials, Mater. Sci. Eng.: B **167**, 6 (2010).

[59] M. Hinterstein, K.-Y. Lee, S. Esslinger, J. Glaum, A. J. Studer, M. Hoffman, and M. J. Hoffmann, Determining fundamental properties from diffraction: Electric field induced strain and piezoelectric coefficient, Phys. Rev. B **99**, 174107 (2019).

[60] L. Lemos da Silva, K.-Y. Lee, S. Petrick, M. Etter, A. Schökel, C. G. Chaves, N. Oliveira da Silva, K. Lalitha, G. Picht, and M. J. Hoffmann, Uncovering the symmetry of the induced ferroelectric phase transformation in polycrystalline barium titanate, J. Appl. Phys. **130**, 234101 (2021).

[61] Q. M. Zhang, H. Wang, N. Kim, and L. E. Cross, Direct evaluation of domain-wall and intrinsic contributions to the dielectric and piezoelectric response and their temperature dependence on lead zirconate-titanate ceramics, J. Appl. Phys. **75**, 454 (1994).

[62] M. Budimir, D. Damjanovic, and N. Setter, Piezoelectric anisotropy–phase transition relations in perovskite single crystals, J. Appl. Phys. **94**, 6753 (2003).

[63] H. Liu, J. Chen, L. Fan, Y. Ren, Z. Pan, K. V. Lalitha, J. Rödel, and X. Xing, Critical Role of Monoclinic Polarization Rotation in High-Performance Perovskite Piezoelectric Materials, Phys. Rev. Lett. **119**, 017601 (2017).

[64] A. Wohninsland, A.-K. Fetzer, R. Broughton, J. L. Jones, and K. Lalitha, Structural and microstructural description of relaxor-ferroelectric transition in quenched $Na_{1/2}Bi_{1/2}TiO_3BaTiO_3$, J. Materiomics **8**, 823 (2022).

[65] H. Baerwald and D. Berlincourt, Electromechanical response and dielectric loss of prepolarized barium titanate under maintained electric bias. Part I, J. Acoust. Soc. Am. **25**, 703 (1953).

[66] A. Nowick and W. Heller, Dielectric and anelastic relaxation of crystals containing point defects, Adv. Phys. **14**, 101 (1965).

[67] K. Carl and K. Hardtl, Electrical after-effects in Pb(Ti, Zr)O_3 ceramics, Ferroelectrics **17**, 473 (1977).

[68] G. Picht, N. H. Khansur, K. G. Webber, H. Kungl, M. J. Hoffmann, and M. Hinterstein, Grain size effects in donor doped lead zirconate titanate ceramics, J. Appl. Phys. **128**, 214105 (2020).

[69] B. Li, M. S. Cao, J. Liu, and D. W. Wang, Domain structure and enhanced electrical properties in sodium bismuth titanate ceramics sintered from crystals with different morphologies, J. Am. Ceram. Soc. **99**, 2316 (2016).

[70] H. J. Lee, S. O. Ural, L. Chen, K. Uchino, and S. Zhang, High power characteristics of lead-free piezoelectric ceramics, J. Am. Ceram. Soc. **95**, 3383 (2012).

Texture-based ferroelectric hardening in $Na_{1/2}Bi_{1/2}TiO_3$-based piezoceramics

Daniel Bremecker[1*], Andreas Wohninsland[1], Siegfried Teuber[1], K.V. Lalitha, Manuel Hinterstein[2,3] and Jürgen Rödel[1+]

[1]*Division of Nonmetallic-Inorganic Materials, Department of Materials and Earth Sciences, Technical University of Darmstadt, 64287 Darmstadt, Germany*

[2]*Fraunhofer IWM, Freiburg, Germany*

[3]*Institute for Applied Materials, Karlsruhe Institute of Technology, Karlsruhe, Germany*

*E-Mail: bremecker@ceramics.tu-darmstadt.de

[+]E-Mail: roedel@ceramics.tu-darmstadt.de

1 Supplementary material

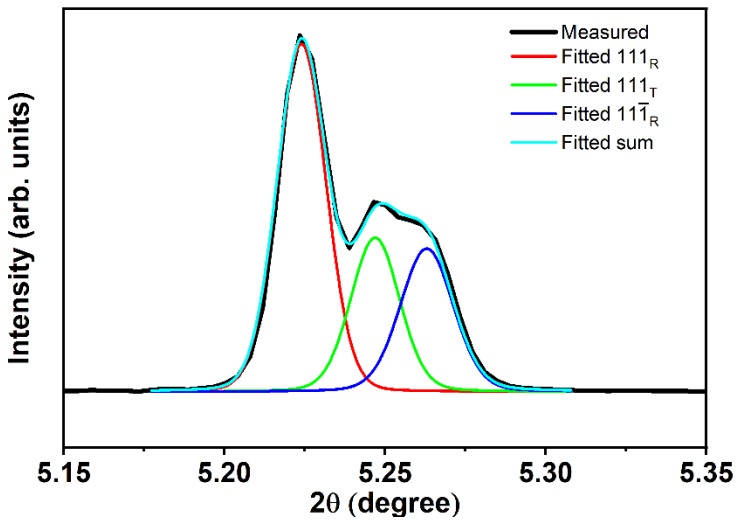

Figure S 1: Measured and fitted 111_{pc} reflection of NBT-6BT-0.5Zn-FC at Ψ=40°.

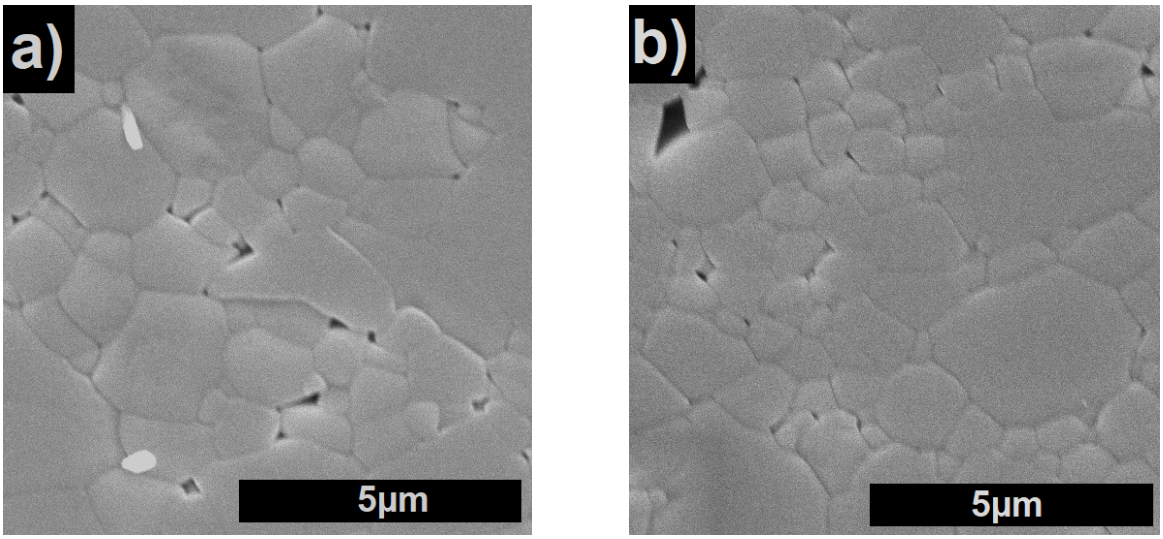

Figure S 2: Microstructure of NBT-21KBT (a) and NBT-21KBT-0.5Mg (b). The micrographs were collected with SEM.

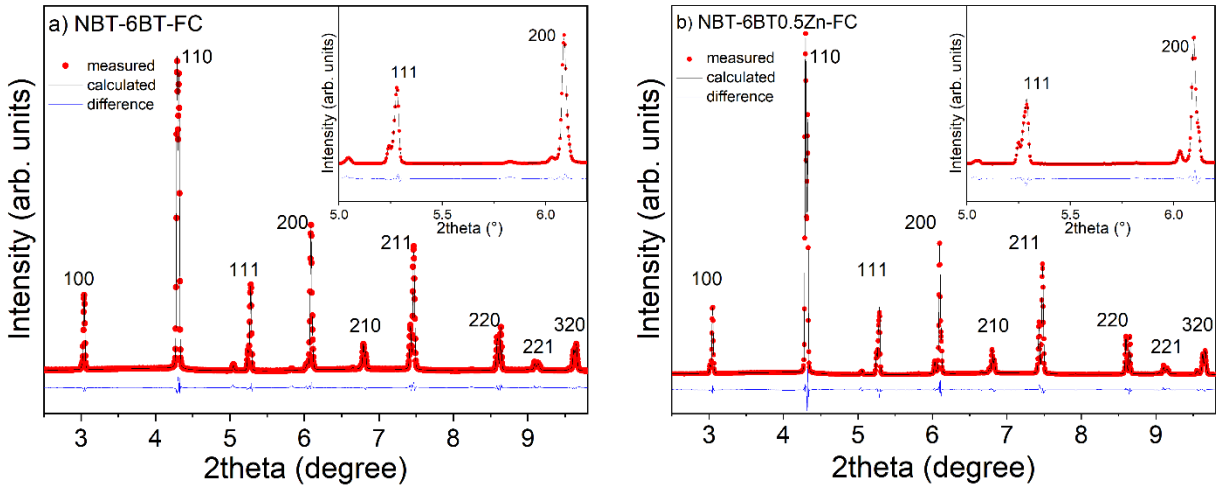

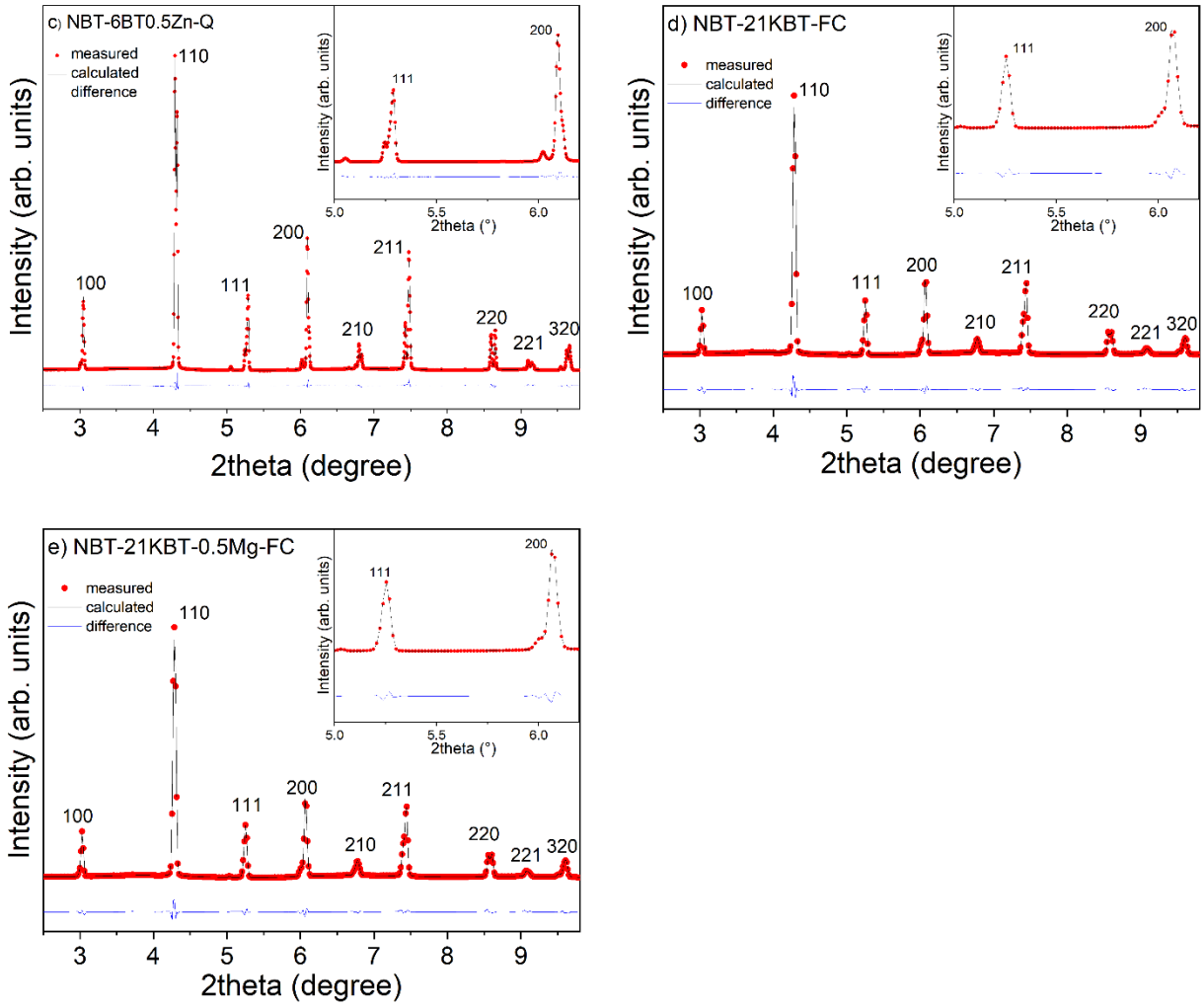

Figure S 3: Measured (red) and calculated (black) X-ray diffraction profiles and respective difference curves of NBT-6BT-FC (a), NBT-6BT-0.5Zn-FC (b), NBT-6BT-0.5Zn-Q (c), NBT-21KBT (d) and NBT-21KBT-0.5Mg (e). The depicted diffraction patterns were collected on poled bulk ceramics.

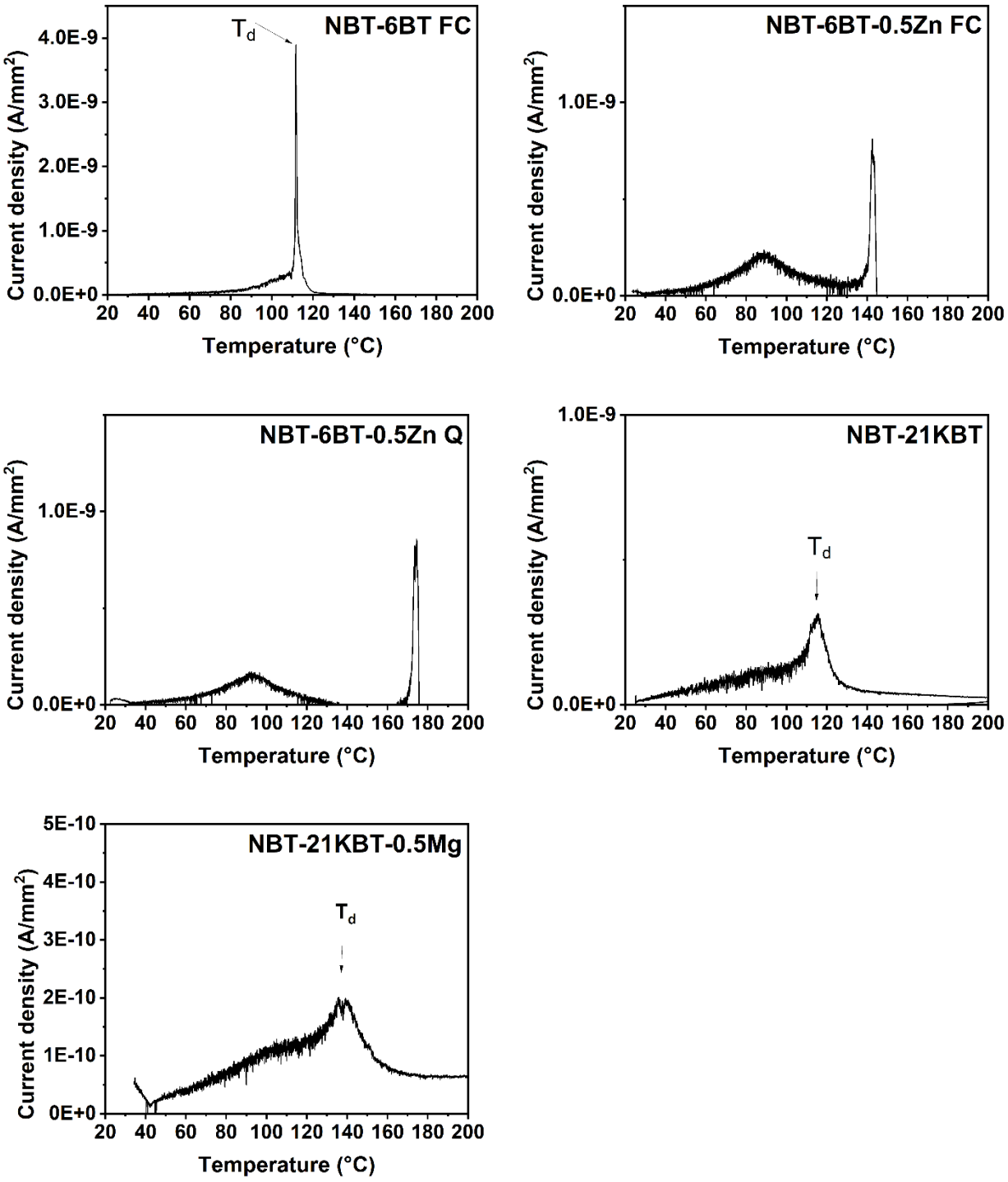

Figure S 4: Thermally stimulated depolarization current of NBT-6BT, NBT-6BT-0.5Zn-FC, NBT-6BT-0.5Zn Q, NBT-21KBT, NBT-21KBT-0.5Mg.

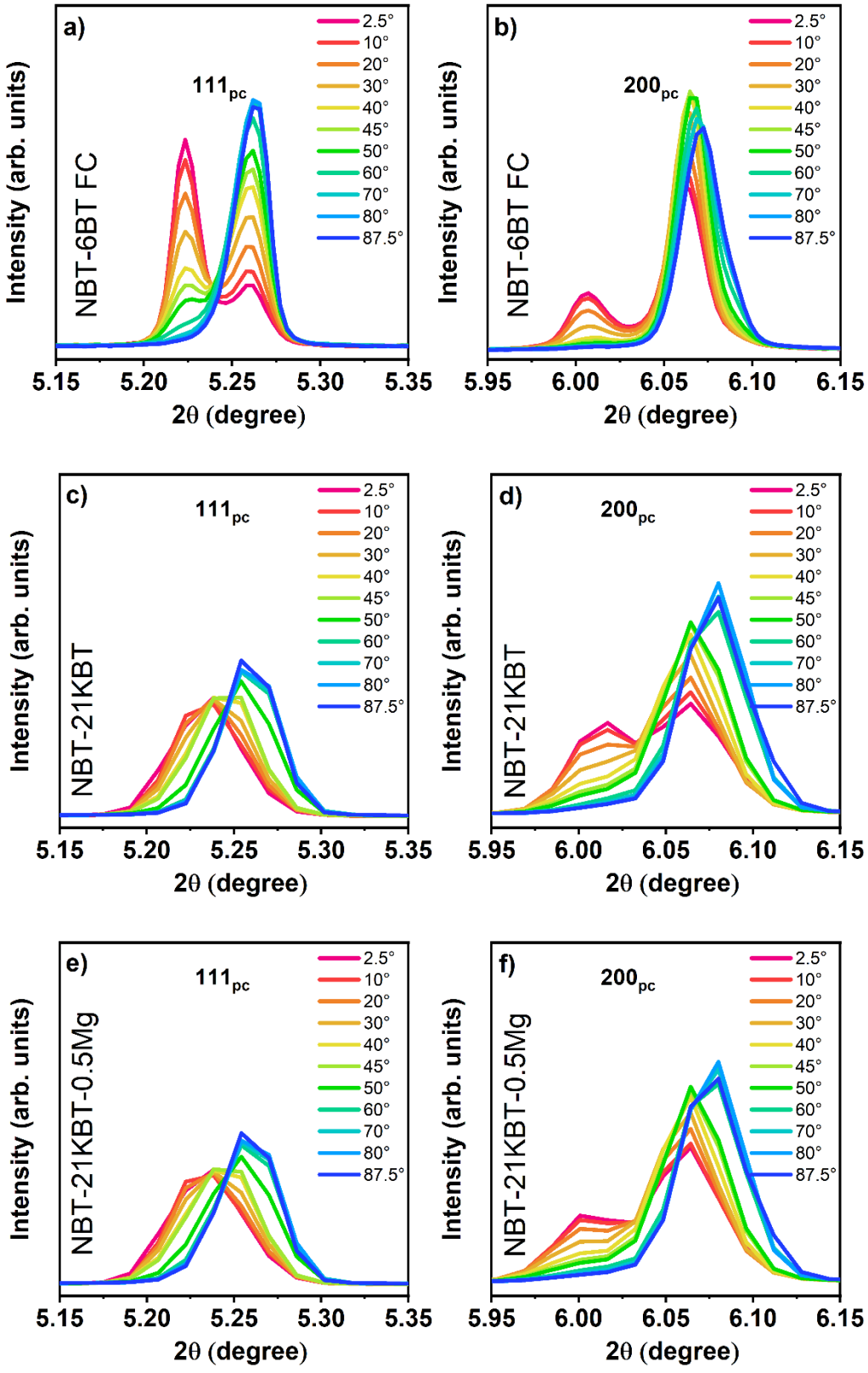
a)
111pc
NBT-6BT FC
Intensity (arb. units)
2θ (degree)
b)
200pc
NBT-6BT FC
c)
111pc
NBT-21KBT
d)
200pc
NBT-21KBT
e)
111pc
NBT-21KBT-0.5Mg
f)
200pc
NBT-21KBT-0.5Mg
2.5°
10°
20°
30°
40°
45°
50°
60°
70°
80°
87.5°
5.15
5.20
5.25
5.30
5.35
5.95
6.00
6.05
6.10
6.15

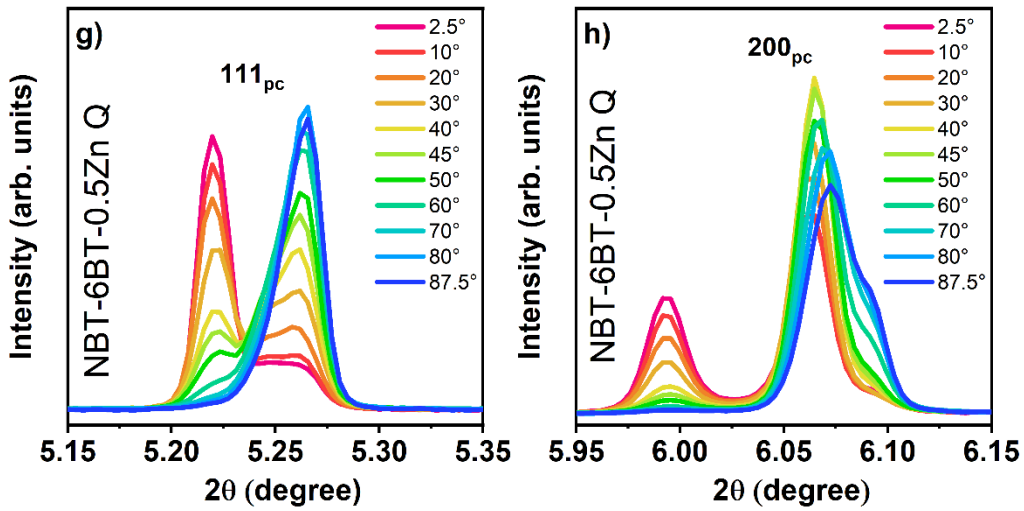

Figure S 5: X-ray diffraction profile of NBT-6BT (a) 111_{pc} (b) 200_{pc}, NBT-21KBT (c) 111_{pc} (d) 200_{pc}, NBT-21KBT-0.5Mg (e) 111_{pc} (f) 200_{pc}, NBT-6BT-0.5Zn-Q (g) 111_{pc} (h) 200_{pc} for different azimuth angles. All samples are measured in the poled state.

$$x_{h=}\frac{\cos\left(\sin^{-1}\left[\frac{k_x}{\sqrt{h_x^2+k_x^2}}\right]\right)}{\tan\left(\frac{\frac{\pi}{2}-\sin^{-1}[l_x]}{2}\right)} \quad (1)$$

$$x_{k=}\frac{\sin\left(\sin^{-1}\left[\frac{k_y}{\sqrt{h_y^2+k_y^2}}\right]\right)}{\tan\left(\frac{\frac{\pi}{2}-\sin^{-1}[l_y]}{2}\right)} \quad (2)$$

$$x_{l=}\frac{\cos\left(\sin^{-1}\left[\frac{k_z}{\sqrt{h_z^2+k_z^2}}\right]\right)}{\tan\left(\frac{\theta_z}{2}\right)} \quad (3)$$

$$y_{h=}\frac{\sin\left(\sin^{-1}\left[\frac{k_x}{\sqrt{h_x^2+k_x^2}}\right]\right)}{\tan\left(\frac{\frac{\pi}{2}-\sin^{-1}[l_x]}{2}\right)} \quad (4)$$

$$y_{k=}\frac{\cos\left(\sin^{-1}\left[\frac{k_y}{\sqrt{h_y^2+k_y^2}}\right]\right)}{\tan\left(\frac{\frac{\pi}{2}-\sin^{-1}[l_y]}{2}\right)} \quad (5)$$

$$y_{l=}\frac{\sin\left(\sin^{-1}\left[\frac{k_z}{\sqrt{h_z^2+k_z^2}}\right]\right)}{\tan\left(\frac{\theta_z}{2}\right)} \quad (6)$$